Chapter 2

Experimental

■■

This chapter discusses various synthesis routes adopted and the characterization techniques used in the thesis work. It also presents a discussion on preparation/fabrication steps involved in Na^+/Li^+ ion all-solid-state supercapacitors (ASSCs).

2.1. Hybrid polymer-NASICON preparation

To prepared these hybrid SPEs, firstly Li^+/Na^+ ion-conducting NASICONs (e.g. $LiTi_2(PO_4)_3$, $Li_{1.3}Ti_{0.7}Al_{0.3}(PO_4)_3$, $NaTi_2(PO_4)_3$, and $Na_3Zr_2Si_2PO_{12}$) were synthesized by conventional solid-state reaction route as described elsewhere [1][2][3] (details in section 2.1.1). Secondly, using fine NASICON nanocrystallites, the hybrid SPEs i.e. polymer-NASICON composites were synthesized by two different techniques (details in section 2.1.2). For all the Na^+ and Li^+ ion systems, PEO was taken as host polymer because of its high cation solvation limit [4] and better conductivity at room temperature due to its properties emphasized in chapter 1.

2.1.1. NASICON synthesis

Two of the Li^+ ion conducting NASICON structured compounds $LiTi_2(PO_4)_3$ (LTP) and $Li_{1.3}Ti_{0.7}Al_{0.3}(PO_4)_3$ (LATP), were chosen for the present study on Li^+ ion CSPEs. Similarly, NASICONs viz. $NaTi_2(PO_4)_3$ (NTP) and $Na_3Zr_2Si_2PO_{12}$ (NZSP) were preferred to develop Na^+ ion-conducting systems. Following the conventional solid-state reaction route as described elsewhere [1][2][3], NASICON particles were synthesized (details in appendix I). In this route, high purity components (Li_2CO_3 /Na_2CO_3, $Al(OH)_3$, TiO_2, ZrO_2, SiO_2, $NH_4H_2PO_4$) were taken in a stoichiometric weight ratio and thoroughly mixed using an agate mortar and pestle, and taken into an alumina crucible (99.99% purity) for calcined at 700°C for 2h and subsequently at 1000°C again for 2h. The resultant powders were manually ground using a pestle and mortar. The formation of NASICON structure was confirmed using powder X-ray diffraction (Rigaku Miniflex II).

The NASICON powders were further ground into fine and homogenous nanoparticles using a planetary ball mill (Fritsch P6). Wet milling was carried out in acetone medium using zirconium/agate pot of 80 ml and balls of 5 mm diameter. To maintain a uniform size of the nanoparticles throughout the study, the mass ratio of ball to sample was kept to 5:1, with milling time ~ 12 h. Prolong milling was avoided to prevent contamination and decomposition. The ball-milled samples were then transferred to 1 glass Petri dish and further dried at room temperature to remove the acetone medium. To confirm the presence of any decomposed product or impurities/contamination due to milling, the synthesis samples were readily characterized using X-ray diffraction. Using the synthesized nanoparticles of NASICON, polymer-NASICON hybrid solid electrolytes were developed via two methods described in sections 2.1.2 and 2.1.3, respectively.

2.1.2. Solution casting method

Polyethylene oxide (PEO) was used as host along with Li^+/Na^+ ion alkali metal salts (NaI, $NaCF_3SO_3$, $LiCF_3SO_3$) and respective NASICONs (LTP, LATP, NTP or NZSP). Due to its hygroscopic nature, alkali metal salt (e.g. $NaCF_3SO_3$, $LiCF_3SO_3$ etc.) was vacuum dried at 100°C for 2h prior to synthesis of the composite. In this route, in stoichiometric weight ratio, the host polymer and alkali metal (Li^+/Na^+ ion-conducting) salts were dissolved in acetonitrile solvent separately in a glass beaker using a magnetic stirrer. After stirring for ~ 6h, polymer matrix and alkali metal solution were blended and stirred for another ~ 6h. Before dispersion, various batches of NASICONs were ultrasonicated in an acetonitrile medium for 30 min to remove aggregation of particles. The nanoparticles were dispersed into the blended matrix of polymer and alkali metal salt. Further, the NASICON dispersed polymer matrices were stirred to obtain a viscous slurry of the composite. The slurry was subsequently poured into a Teflon Petri dish and kept overnight at 40°C to remove the residual solvent.

This way series of Li^+ and Na^+ ion based hybrid polymer-NASICON composites were prepared. In the preparation of composites, two strategies were adopted viz. (i) keeping salt constant and varying NASICON content in the matrix, (ii) fixing NASICON to a particular value and varying salt content on the cost of PEO in the matrix. The sets of Li^+/Na^+ ion conducting hybrid polymer-NASICON composites prepared for the present study are as follows:

(i) $5LiCF_3SO_3-95[PEO_{1-x}(LiTi_2(PO_4)_3)_x]$ where, $0 \leq x \leq 0.9$.

(ii) $5LiCF_3SO_3-95[PEO_{1-x}(Li_{1.3}Al_{0.3}Ti_{1.7}(PO_4)_3)_x]$ where, $0 \leq x \leq 0.7$.

(iii) $10NaI-90[PEO_{1-x}NTP_x]$ where, $0 \leq x \leq 0.7$.

(iv) $10NaCF_3SO_3-90[NTP_xPEO_{1-x}]$ where $x = 0$, 0.4 and 0.7

(v) $63Na_3Zr_2Si_2PO_{12}-37(PEO_{1-x}NaI_x)$ for $x = 0.03 - 0.13$

To obtain a free-standing and uniform thickness film, the polymer-NASICON hybrid composite obtained via solution casting was further hot pressed, particularly for compositions with lesser NASICON content viz. $x \leq 0.4$. The films were sandwiched between Teflon sheets with stainless steel spacer of 250 μm to maintain the thickness and further heated in a polymer press at ~ 2 tons-cm^{-2} (Hydraulic press PF-M15) to melt the polymer at ~ 80°C for 15 min. Further, the sample was naturally cooled down using water circulation in the heating plate. The obtained free-standing films were kept in a vacuum oven at ~ 40°C for 1 day to remove stresses and later stored in a vacuum desiccator.
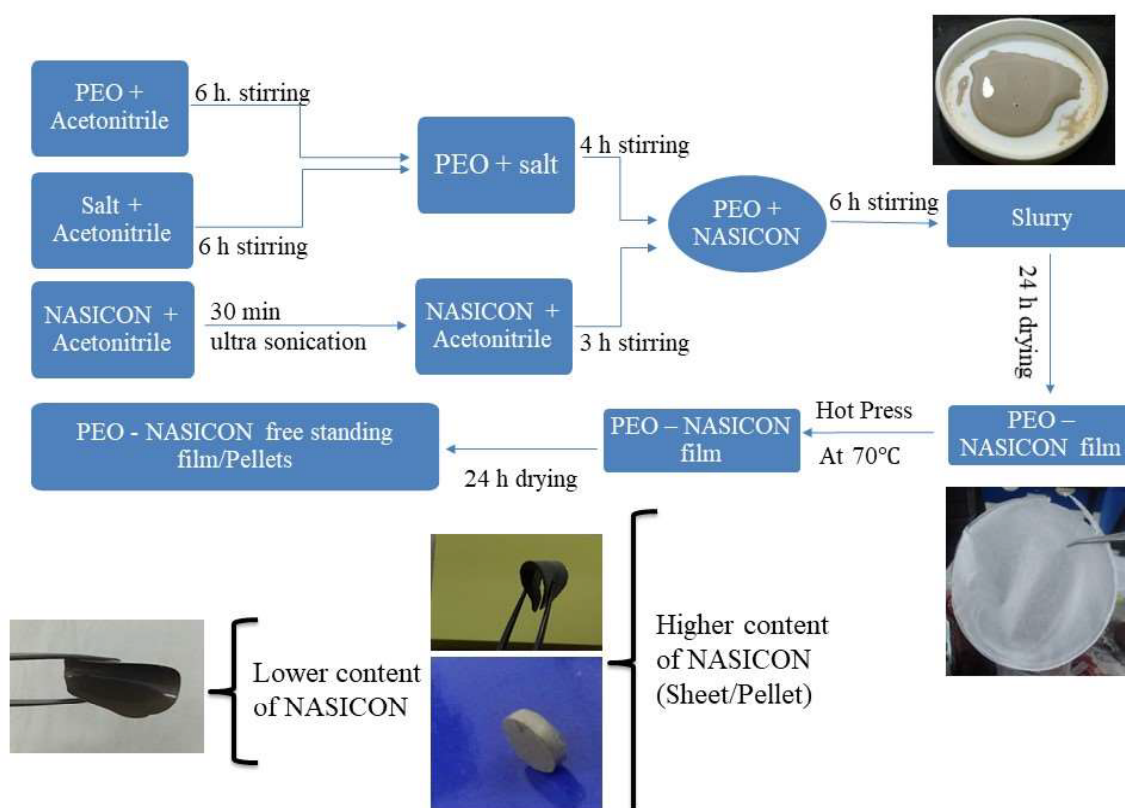
Figure 2.1 *Schematic diagram for the synthesis of hybrid polymer-NASICON electrolyte adopted for Li$^+$ and Na$^+$ ion-based systems.*

■ ■

For composites with large NASICON content $x \geq 0.4$, it was not possible to obtain freestanding films, thus slurry was dried and pelletized with 2 ton-cm^{-2} pressure using a stainless steel die (8 -10 mm diameter). Pellets were subsequently heat treated in a vacuum oven at 40°C for 24 h to remove stresses due to pressure. The obtained pellets of the composite were also kept in a vacuum desiccator for further characterization. A schematic diagram for the synthesis roadmap is shown in Fig 2.1.

2.1.3. One-pot synthesis route

A novel approach for the synthesis of Hybrid polymer-NASICON electrolytes was adopted to develop NASICON dispersed solid polymer electrolytes with better homogeneity [5]. In this synthesis route, an appropriate stoichiometric weight ratio of polymer, NASICON nanocrystallites, and salt were taken into a zirconium pot (80 ml) with balls (10 mm diameter) in acetonitrile as a solvent. Similar to the earlier synthesis route, alkali metal salt was vacuum dried at 100°C for 2 h, and NASICON nanoparticles were separately ultrasonicated for ~ 15 min. The mixture of the composite was subsequently balled milled for ~24h until a viscous slurry is formed. The obtained viscous slurry was again dried in Teflon petri dish for ~ 24h, and further vacuum dried at 40°C for another~24h to remove the residual solvent.

Figure 2.2 *Schematic diagram of one-pot synthesis route*

Flexible solid polymer electrolyte films of thickness ~ 250 μm were prepared using a polymer hot press for the sample with x ≤ 0.4. For samples with x > 0.4, relatively thicker sheets of 450μm were prepared (as shown in Fig.1). The resultant films were kept in a vacuum desiccator at 40°C for 1 day to remove stresses and later used for further characterization and device fabrication. A schematic diagram of the synthesis technique is shown in Fig.2.2. The Na^+ ion-based composites viz. $10NaI-90[PEO_{1-x}(Na_3Zr_2Si_2PO_{12})_x]$ where, $0 \leq x \leq 0.7$ were prepared by this route, particularly for supercapacitor applications. A detailed discussion on the electrical, structural and thermal properties of the composites will be discussed in chapter 4.

## 2.2. Supercapacitor fabrication.

Application potential as an electrolyte for supercapacitor was examined as an electrolyte for all-solid-state supercapacitors (ASSCs).

2.2.1. Electrode for EDLCs

For EDLCs electrodes, activated carbons (ACs) having high specific surface area were vastly used. In order to develop the pore network in carbon materials, physical or chemical activation is often required. Chemical activation is generally achieved by mixing carbonaceous materials (coconut shell, rice husk, tea, etc.) with chemical activating agents (KOH, H_3PO_4, $ZnCl_2$, etc.), followed by the carbonization at 400-900°C. This process gives rise to porous carbons. Among various chemical reagents, KOH is widely used since it leads to ACs with defined micropore size distribution, high micropore volume, and a very high specific surface area. The activation process below 700°C was performed that leads to the following sequence of reactions [6],

$$2KOH \rightarrow K_2O + H_2O$$
$$C + H_2O \rightarrow CO + H_2$$
$$CO + H_2O \rightarrow CO_2 + H_2$$
$$CO_2 + K_2O \rightarrow K_2CO_3$$
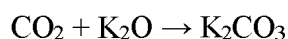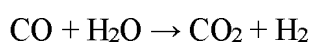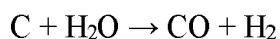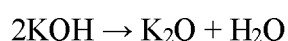
Above 700°C, the following reactions take place that leads to the formation of sub-nanometer pores [7].

$$K_2O + H_2 \rightarrow 2K + H_2O$$
$$K_2O + C \rightarrow 2K + CO$$
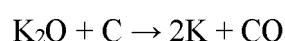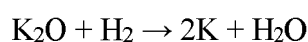
In the present study, activated carbon was prepared using crushed coconut shell. Fine powders of the coconut shell were mixed with activating agent KOH in a weight ratio of 1:2 using mortar and pestle. Then the mixture was transferred into an alumina crucible and chemical activation was carried out at 700°C in N_2 atmosphere for 6h. The resulting material was extensively washed in distilled water until the pH of outlet water reached 7.0, and subsequently dried in a vacuum oven to remove the residual water content. Before electrode fabrication, the activated carbon was dry milled for 6h using tungsten pot and balls at 100 rpm to obtain a homogenous distribution of particle size. Further, the samples were subsequently characterized using BET surface area analyzer (BELSORP MINI X) to confirm the specific surface area, pore-volume, and distribution. Optimized samples were considered for device fabrication.

2.2.2 Electrodes for pseudo capacitor

Oxide materials such as MnO_2, NiO, CoO_2 etc. have been widely studied as supercapacitor electrodes because of their unique physical and chemical properties. In recent years MnO_2 has been widely used because of its presence leading to high capacitance and large energy storage, abundance in nature, very low inherent toxicity, high energy storage, environmentally friendliness, and low cost. It has a layered or tunnel-shaped crystal structure that can facilitate the diffusion/intercalation of ions into the bulk material. Its conductivity is though low (10^{-4}-10^{-6} Ω^{-1}-cm^{-1}), interestingly, it can be further modified by combining with multiwalled carbon nanotubes (MWCNT) that have high electrical conductivity and mechanical strength [8].

In the present study, MnO_2/MWCNT were synthesis by hydrothermal route in certain ratios. In this route, $KMnO_4$ and MWCNT were taken in 20 ml distilled water and stirred using a magnetic stirrer for 3-4 min, and subsequently transfer into the Teflon lined stainless steel autoclave (50 ml). The autoclave was heated in a furnace for 3 h at 160°C. The obtained MnO_2 functionalized MWCNT were vacuum dried (U tech) at room temperature prior to electrode fabrication.

2.2.3. EDLCs and Pseudo SCs

Firstly, All-solid-state supercapacitors were fabricated using activated carbon (AC) as an electrode and well-optimized polymer-NASICON hybrid films as electrolyte. The thick slurry of electrode material was prepared by taking activated charcoal, acetylene black, and binder

PVdF-HFP in a ratio of 80:10:10 in 1-Methyl-2-pyrrolidinone (NMP) solvent followed by stirring for ~ 12h. This slurry was coated on two different current collector sheets, viz copper and graphite via doctor blade technique. The thickness of the carbon electrodes on the current collector was kept to ~200 μm. The electrodes were cut into 14 mm diameter and the mass of the carbon composite on the electrodes was 0.6 mg-cm^{-2}. The as-prepared electrodes were vacuum-dried overnight at 100°C prior to EDLC fabrication. EDLCs were fabricated in a 2032 coin cell assembly (Coin cell crimper, Ranga tech). The well-optimized 15 mm diameter and 0.2 mm thickness hybrid polymer-NASICON films were used as electrolyte. A schematic diagram of 2032 cell fabrication and assembly is shown in Fig. 2.3.

(a)   (b)
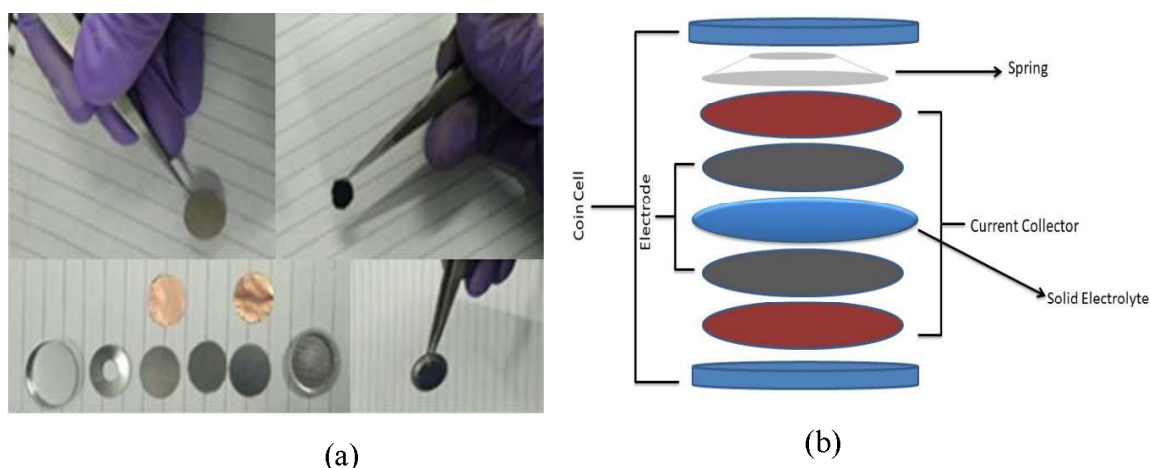
Figure 2.3 *(a) Schematic diagram of EDLC fabrication and (b) coin cell assembly*

Secondly, similar to EDLCs fabrication, pseudo-SCs were also fabricated in 2032 coin cell assembly. The electrodes were prepared by mixing the MnO$_2$/MWCNT with PVdF and acetylene black in a ratio of 80:10:10 in a magnetic stirrer.

## 2.3. Characterization techniques

The structural, surface morphology, thermal, electrical, and chemical bonding properties of the developed hybrid polymer-NASICON electrolyte were characterized using various techniques. Also, the device performances were studied using the electrochemical workstation (AutoLab M204 with CV, EIS and GCD modules). A brief discussion on each technique is now presented below.

2.3.1. X-ray diffraction.

X-ray diffraction (XRD) is one of the most useful techniques to evaluate the crystalline structure, the ratio of crystalline to non-crystalline (amorphous) regions, crystal size, the arrangement pattern of crystals, and the distance between the planes of the crystal. The technique is based on Bragg's diffraction law (Fig. 2.4a) that relates the wavelength of the X-rays to the interatomic spacing, and is given by the following equation:

$$2d\sin\theta = n\lambda \qquad (1)$$

where d is the perpendicular distance between pairs of adjacent planes, θ is the angle of incidence or Bragg angle, λ is the wavelength of the X-rays beam, and n denotes the order of the reflection. Block diagram of XRD set up is shown in Fig. 2.4b.

(a)   (b)
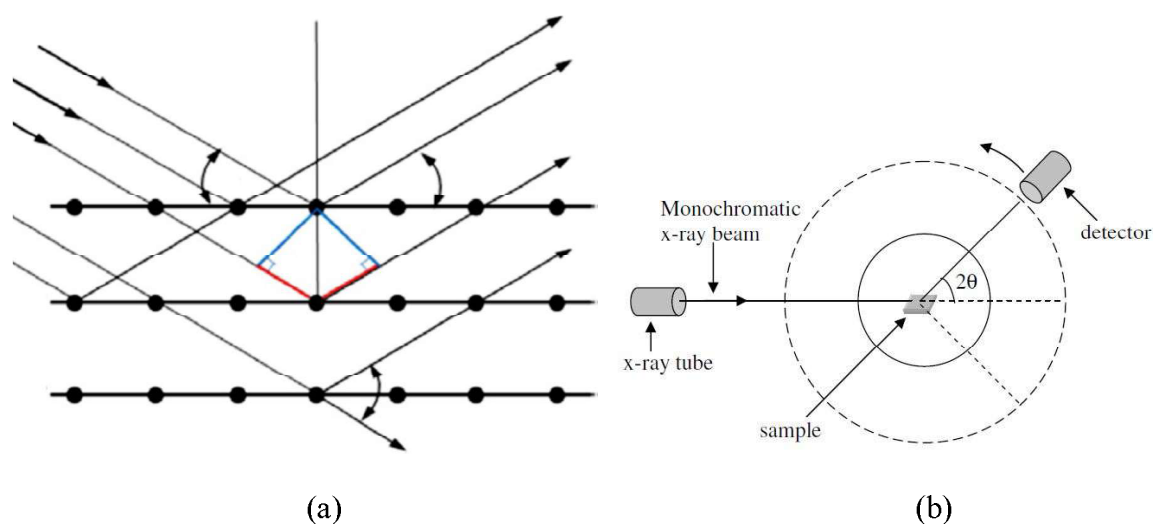
Figure 2.4 (a) Geometrical representation of Bragg's law. (b) Block diagram of XRD setup.

In the present study, an X-ray diffractometer (Rigaku MiniFlex II, X-Ray source: Cu Kα; 1.54 Å) was used to characterize the hybrid polymer-NASICON electrolyte. The XRD scans were carried out (10-90 degrees of 2θ) with a scan rate of 1°-min^{-1} with a step size of 0.005 degrees. From the diffraction patterns, the crystallite size was also calculated using Debye Scherrer's relation as given below.

$$\text{Crystallite size} = \frac{0.91\,\lambda}{\beta\cos\theta}$$

Using the X-Ray diffraction technique, the formation of the NASICON phase and their crystallite size was confirmed. Also, the effect of NASICON content in the crystalline phase of polymer PEO was studied. Using equation 2, the crystallite size of the polymer, Scherrer length [9], was also studied for various composites with NASICON content.

2.3.2. Differential Scanning Calorimetry (DSC)

Differential scanning calorimetry (for the present study Shimadzu DSC 60) is a useful tool for thermal analysis of polymer composites using changes in heat capacity that results due to exothermic or endothermic thermal events (reactions) in the sample. It can be used to identify the glass transition (T_g) and melting event (T_m) of polymer composites. The instrument measures the difference in the heat flow between the sample and the reference. A schematic instrumental setup of DSC is shown in Fig. 2.5a.

(a)   (b)
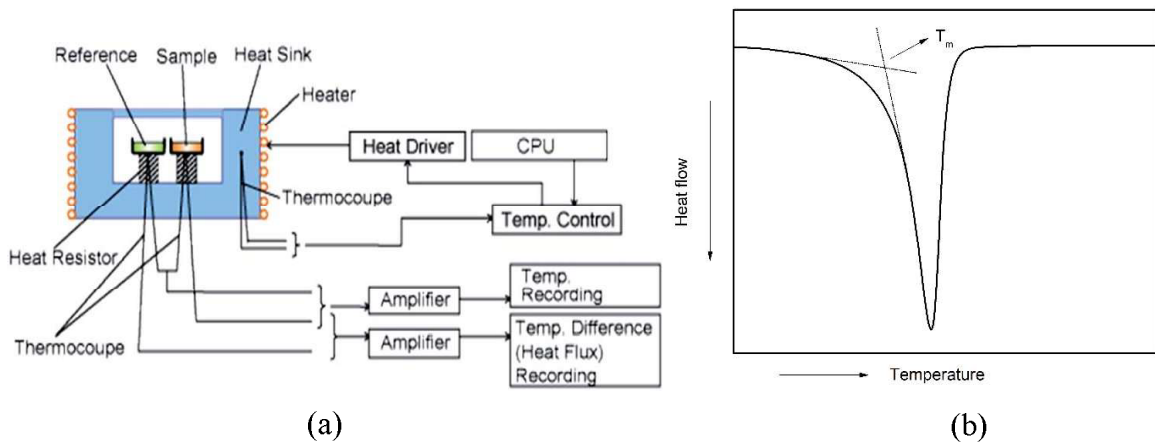
Fig. 2.5 *(a) Block diagram of DSC set up (after stark et. al. [10]) and (b) A schematic DSC scan of a typical CSPE*

The temperature of the thermal event (T_m, T_g, T_c) was determined from the onset of the transition as shown in Fig. 2.5b. The degree of crystallinity in the polymer is an important factor to determine the composite's properties, which was evaluated by measuring the enthalpy of melting and comparing with the enthalpy of melting for the pure polymer [11] as given in the equation

$$\text{Fraction of crystallinity} = \frac{\Delta H_{CPE}}{\Delta H_{Polymer}} \qquad (3)$$

Where ΔH is the enthalpy of melting obtained from the area under the DSC thermogram.

53

2.3.3. Field Emission Scanning Microscope (FESEM)

Field emission scanning electron microscopy (FE-SEM) is a powerful imaging tool that is used to investigate the surface morphology (e.g., particle size and shape), imperfections, and topology of nanocrystalline powders and bulk materials. This technique is also used to investigate the elemental distribution within the composite/compound on a submicron scale.

A block diagram of the FESEM setup is shown in Fig. 2.6. When primary electrons which are liberated from source bombard the sample, secondary electrons are emitted. The angle and velocity of these secondary electrons bring information about the surface structure of the object. A detector catches the secondary electrons and transformed the information to a digital image [12].
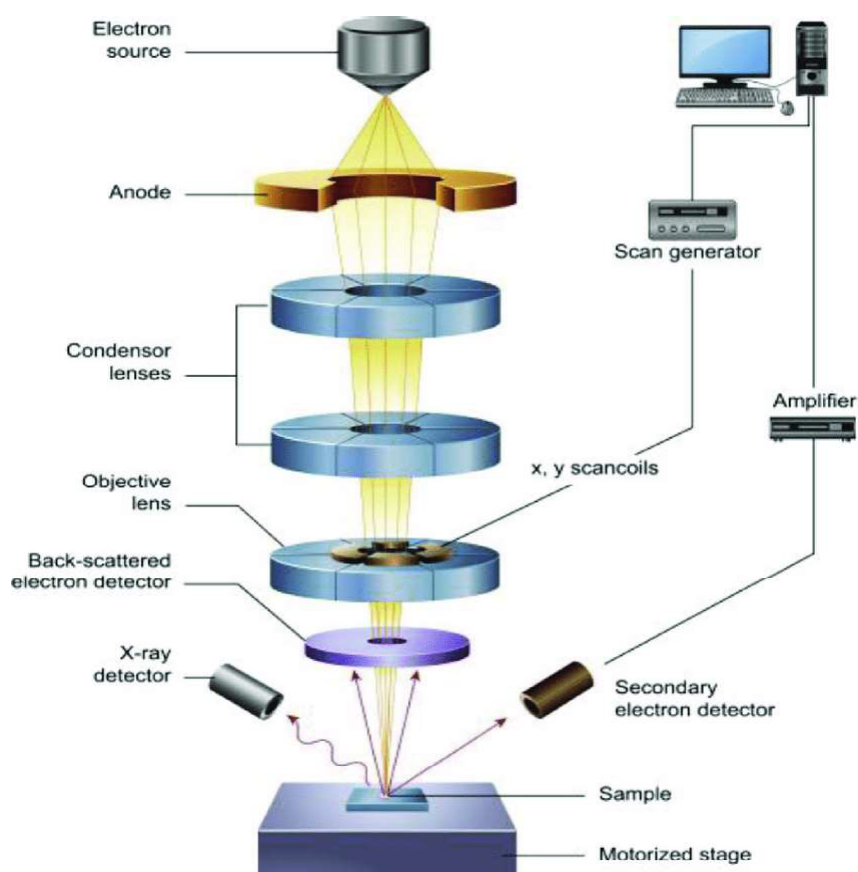
Figure 2.6 *Block diagram of FESEM instrument set up (after Mayeen et. al. [12]).*

In the present work, the surface morphology of the polymer-NASICON hybrid composites was investigated by field emission scanning electron microscopy, FESEM (FEI-Apreo-S). The surface of the samples was first made conductive by a gold coating of 1.5 -3 nm. Images were

taken by using 20 kV accelerating voltage. Using this technique, the NASICON embedded structure was studied.

Energy Dispersive X-ray Spectroscopy (EDX or EDS) is a powerful technique used to identify the elemental composition of the material that is attached to the FESEM. It works by detecting X-rays that are produced by a sample placed in an electron beam. The electron beam excites the atoms in the sample that subsequently produces X-rays to discharge the excess energy. The energy of X-ray is a typical characteristic of an atom that produces it. As the electron beam can be precisely controlled, the beam can sweep over a selected area of the sample to identify the elements in that region. In the current work, X-ray mapping was acquired for the composites to understand the qualitative elemental distribution across the specimen to comprehend the homogeneity of NASICON distribution in the polymer-NASICON composites.

2.3.4. Soft X-ray absorption spectroscopy (SXAS)

X-rays in a particular range of spectrum have sufficient energy to eject one or more core electrons from an atom. Each core electron has well-defined binding energy, and when the energy of the incident X-ray is scanned across one of these energies, there is an abrupt increase in the absorption coefficient. This is the well-known 'absorption edge' of the element, as shown in Fig. 2.7b. In XAS interesting information is obtained from X-rays absorbed by an atom at energies near and above the core-level binding energies [13]. It is thus used to investigate the local structural environment of various atoms (elements) in composites. The technique can be divided into X-ray absorption near edge structure (XANES), and extended X-ray absorption fine structure (EXAFS), as shown in Fig 2.7b. As the technique probes beyond the crystal structure, it is one of the best structural probes available for investigating non-crystalline/highly disordered materials as well.

The core electron can be excited into unoccupied bound, or continuum states, as shown in Fig. 2.7a. The key fact is that the photoelectrons act as very sensitive probes that can feel the charge distribution and the arrangement of the neighboring atoms around the absorbing core atom. The low-energy portion of the spectra is known as X-ray absorption near edge structure (XANES). This near-edge structure ends approximately where the electron wavelength equals

the distance from the absorbing atom to its nearest neighbors, about 40–50 eV above the edge [13].
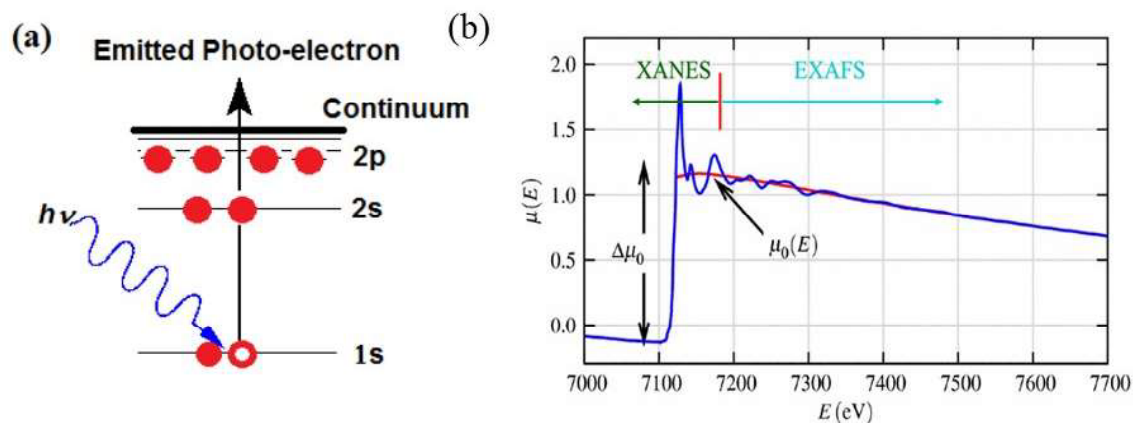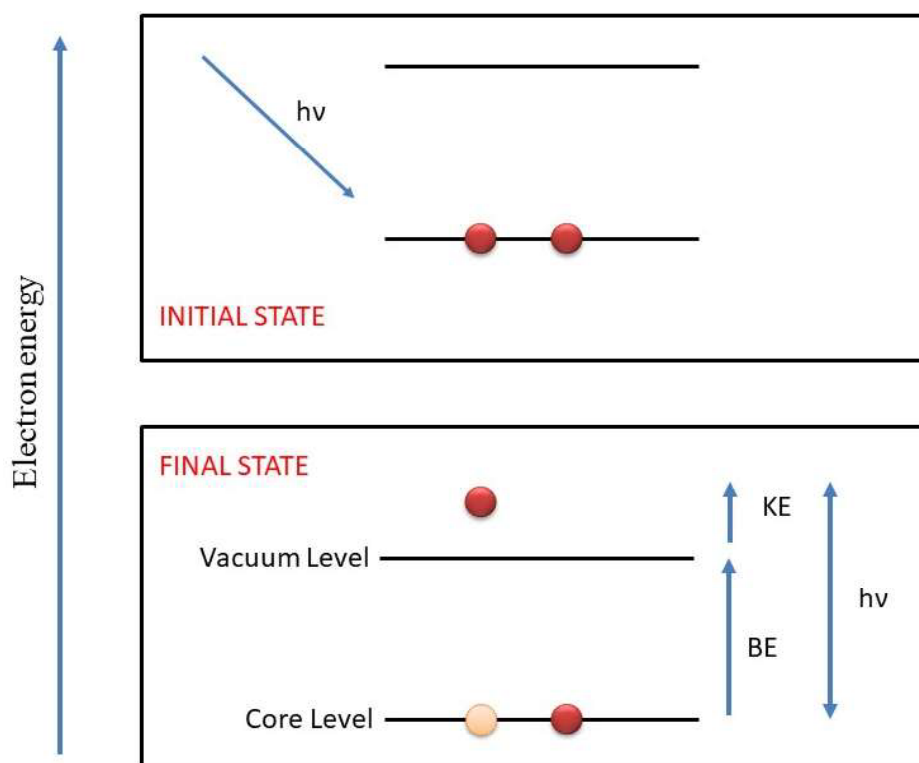

Figure 2.7 *(a) Electron excitation process scheme and (b) XAS spectra including both X-ray Absorption Near Edge Structure (XANES) and Extended X-ray Absorption Fine Structure (EXAFS) (after Garner et al [14])*

In the XANES region, the kinetic energy of the electron is small and the scattering from neighboring atoms is stronger than at higher energies [15]. XANES strongly depends on the local geometry of the material (coordination number and ligand symmetry). The pre-edge region feature is caused by electronic transitions to empty bound states and provides information about the absorber's local geometry, electronic state around the absorber, number of neighbors, ligand symmetry, and valence state. The edge energy can be defined as the energy at some specific absorbance (i.e. half maximum), or can also be taken as the energy of the first inflection point [15]. The edge energy typically increases by several eV per oxidation unit.

XANES can provide excellent quantitative information about change in the charge state of a particular element due to the presence of other atoms around it. In the present study, to understand the ion-ion interaction between ether oxygen of PEO and Li^+/Na^+ ion, X-ray absorption near-edge structure (XANES) spectroscopy were studied for oxygen K-edge and titanium L-edge using the synchrotron radiation facility, Indus-II beamline-01 (100–1100 eV) at Raja Ramanna Centre for Advanced Technology (RRCAT), Indore (India). The measurements were carried out in a total electron yield (TeY) mode for all compositions, and data from the beamline were processed using ATHENA software.

2.3.5. X-ray Photoelectron spectroscopy

X-ray photoelectron spectroscopy (XPS) is a powerful, non-destructive analytical tool for understanding the basics of electronic and band structures of atoms and molecules on the surface of solids [16]. In particular, XPS has been effectively utilized in the characterization of material surfaces and specific areas of materials science such as polymer chemistry, corrosion, and composite materials.

 The XPS technique is highly surface specific due to the short range of the photoelectrons that are excited from the solid. The energies of the photoelectrons leaving the sample are determined using a concentric hemispherical analyzer and this gives a spectrum with a series of photoelectron peaks. The binding energy (BE) of the peaks is characteristic of each element. The peak areas can be used to determine the composition of the material's surface. The shape of each peak and the BE can be slightly altered by the chemical state (charge state) of the emitting atom. Hence XPS can provide chemical bonding information as well.

Figure 2.8 Electron excitation process.

The photoemission process from a solid sample takes place when a highly energetic photon interacts with matter, causing an electron to be removed from an atomic orbital, or from a band

■ ■

to reach the vacuum level [17] as shown schematically in Fig. 2.8. When an atom or molecule absorbs an X-ray photon, an electron can be ejected. The kinetic energy (KE) of the electron depends upon the photon energy (hυ) and the BE of the electron as given in the below equation.

$$KE = hυ - (BE + \Phi) \qquad (4)$$

In the present study, synchrotron-based X-ray Photoelectron Spectroscopy (XPS) measurements were carried out at beamline 14, Indus II (2.5 GeV beam energy and stores current up to 200 mA), RRCAT Indore, India. A monochromatic beam with excitation energy of 4.4 keV with 160 mA current was used for characterization. X-ray photoelectron acquisition was carried out using SpecsLab Prodigy (15 keV resolution) Model [18]. The measurements were carried out for all the compositions in individual run mode for oxygen, as per our interest. Further, to ensure a constant error in energy calibration, individual scans of all compositions were carried out in one shot. HSA 15,000 Hemispherical Analyzer was used for accurate current measurement. XPS spectra were analyzed using CasaXPS software (version 2.3.19).

2.3.6. BET surface area analysis

By BET (Brunauer, Emmett, and Teller) technique [19], the *specific surface area* of a sample is measured – including the pore size distribution. The specific surface determined by BET relates to the total surface area (reactive surface) as all porous structures adsorb the small gas molecules. The specific surface area is determined by the physical adsorption of a gas on the surface of the solid, and by calculating the amount of adsorbate gas corresponding to a monomolecular layer on the surface. Physical adsorption results from relatively weak (van der Waals) forces (at 77K) between the adsorbate gas molecules and the adsorbent surface area of the test powder. The amount of gas adsorbed can be measured by a volumetric or continuous flow procedure. The data are treated according to the Brunauer, Emmett, and Teller (BET) adsorption isotherm equation:

$$\frac{1}{[V_a(\frac{P_o}{P}-1)]} = \frac{C-1}{V_m C} \times \frac{P}{P_o} + \frac{1}{V_m C} \qquad (4)$$

Where, P is the partial vapour pressure (pascals) of adsorbate gas in equilibrium with the surface at 77.4 K (b.p. of liquid nitrogen), P_o is the saturated pressure of adsorbate gas, in Pascals, V_a is the volume (im mL) of gas adsorbed at standard temperature and pressure (STP)

■ ■

[273.15 K and atmospheric pressure (1.013×10^5 Pa)], V_m is the volume (mL) of gas adsorbed at STP to produce an apparent monolayer on the sample surface, and C is the dimensionless constant that is related to the enthalpy of adsorption of the adsorbate gas on the powder sample.

When $\frac{1}{[V_a(\frac{P_o}{P}-1)]}$ is plotted against P/P_o according to equation (4). This plot yield a straight line usually in the approximate relative pressure range 0.05 to 0.3 mbar. The data are considered acceptable if the correlation coefficient, r, of the linear regression is not less than 0.9975; that is, r^2 is not less than 0.995. From the resulting linear plot, V_m and C are thus calculated. Furthermore, the specific surface area, S, in $m^2 \cdot g^{-1}$, is obtained using the equation:

$$\text{Specific surface area} = \frac{V_m N a}{m \times 22400} \qquad (5)$$

Where, N is the Avogadro constant (6.022×10^{23} mol^{-1}), a is the effective cross-sectional area (m^2) of one adsorbate molecule, (0.162 nm^2 for nitrogen), m is the mass of test powder (in grams), and 22400 is the volume occupied by 1 mole of the adsorbate gas at STP allowing for minor departures from the ideal, in milliliters

2.3.7 Impedance Analysis

Impedance spectroscopy (IS) is a powerful technique that utilizes an AC signal to excite or perturb a system under investigation and measure the response (current or voltage). Using the measured data the real and imaginary impedances are calculated and plotted against each other over different perturbation frequencies (impedance spectra). IS data can be employed to measure quantitatively the electric and dielectric properties in the bulk and interfacial regions of solid and liquid materials, including membranes.

In this technique, a small amplitude of sinusoidal (a.c) signal of V = $V_0\, e^{j\omega t}$ is applied to perturb the system and the frequency response output current I = $I_0\, e^{j\omega t+\theta}$ is recorded [20]. According to Ohm's law, Impedance (Z) of the circuit at any frequency (ω) can be represented by [21]

$$Z^* = \frac{V}{I} = \frac{V_0\, e^{j\omega t}}{I_0\, e^{j\omega t+\theta}} \quad = \frac{V_0}{I_0} e^{-j\theta} \qquad (6)$$

$$\text{Also, } Z^* = Z \cos \theta - j\, Z \sin \theta \qquad (7)$$
$$= Z' - j\, Z'' \text{ Where, } Z' = Z \cos \theta \text{ and } Z'' = Z \sin \theta$$

Where Z' and Z" are respectively real and imaginary parts of the impedance. The phase difference θ is represented by

$$\theta = \tan^{-1}(Z''/Z') \qquad (8)$$

The impedance spectroscopy is also used to measure the behavior of the materials in terms of complex permittivity (ε^*), complex modulus (M^*) and complex conductivity (σ^*) (Table 2.1).

Table 2.1 The interrelationship of the three formalisms of impedance spectroscopy.

	Symbol	Relation	Complex form
Impedance	Z^*	$(V_o/I_o)\, e^{-j\theta}$	$Z' + jZ''$
Conductivity	σ^*	$L/(Z^* A)$	$\sigma' + j\sigma''$
Modulus	M^*	$j\omega C_o Z^*$	$M' + jM''$
Permittivity	ε^*	$1/j\omega C_o Z^*$	$\varepsilon' + j\,\varepsilon''$

The impedance and conductivity representations were used for analyzing the electrical behavior of the sample in terms of bulk resistance (R) and its electrical equivalent circuits. The complex permittivity and modulus representations are used for analyzing the dielectric response of the sample.

In the present study, the electrical properties of composite films were studied by using an Impedance analyzer (Hioki IM 3570) in a frequency range 4 Hz-5 MHz. The composite films/pellets were sandwich between stainless steel (SS) electrodes and temperature-dependent electrical properties were studied by keeping the sample holder in a PID-controlled furnace. The schematic diagram of the sample holder and measurement arrangement is shown in Fig 2.9.

These measurements were carried out in (i) static mode, where frequency-dependent ionic conductivity was obtained with temperature, and also in (ii) dynamic mode, where temperature dependence of ionic conductivity (1 kHz) was measured at a heating rate ($\sim$ 1°C/min). The complex conductivity (σ^*) of the composites were calculated using the equation given below.

$$\sigma^* = \frac{l}{Z^*A} \qquad (9)$$

On simplifying,

$$\sigma^* = \frac{l\,cos\theta}{|Z|A} - j\,\frac{l\,sin\theta}{|Z|A}$$

$$= \sigma' - j\,\sigma'' \qquad (10)$$

Where l and A are the length and cross-sectional areas of the sample, respectively. The real and imaginary parts of the σ^* define the ac conductivity and conductivity loss of the composite respectively.
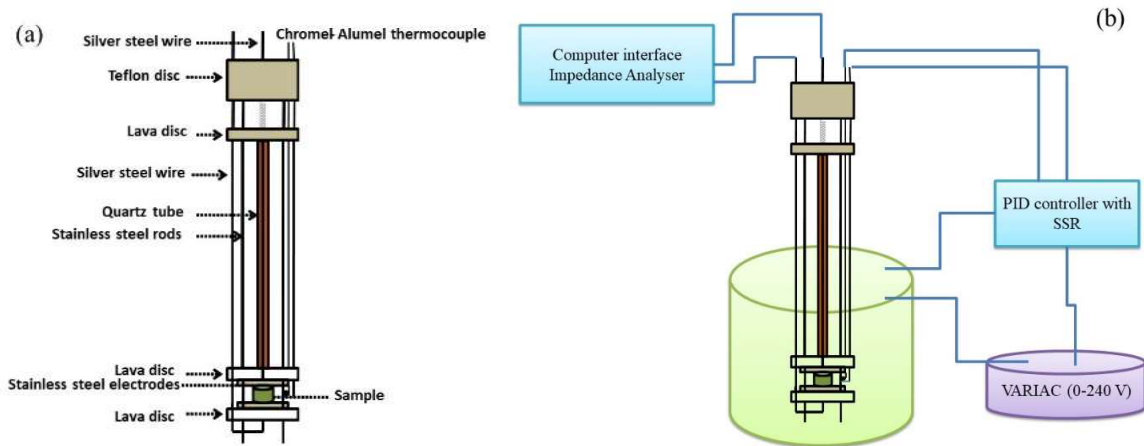

Figure 2.9 *Schematic diagram of (a) sample holder, and (b) IS measurement setup.*

A typical σ' - ω plot for ionic conducting SPEs is shown in Fig 2.10. This plot generally exhibits three regions: in region I, conductivity exhibits a drastic fall essentially due to polarization. In region II, conductivity almost saturates for a wide range of frequency refers to the long-range diffusive motion of ions. The value at the plateau is referred to as dc conductivity. At higher frequencies (III region), it exhibits a dispersion. This region corresponds to short-range ionic motion. This behavior of conductivity spectra obeys the universal Jonscher power law (JPL) characteristics [20] as:

$$\sigma = \sigma_{dc} + A\omega^n \qquad (11)$$

where σ_{dc} is the frequency-independent conductivity (at plateau), A is the pre-exponential factor and n is the fractional exponent and generally lies between 0 and 1. The value of exponent n infers about the different types of ion conduction processes occurring in disordered

materials. This relationship was derived, as a special case, for materials in which the a.c.
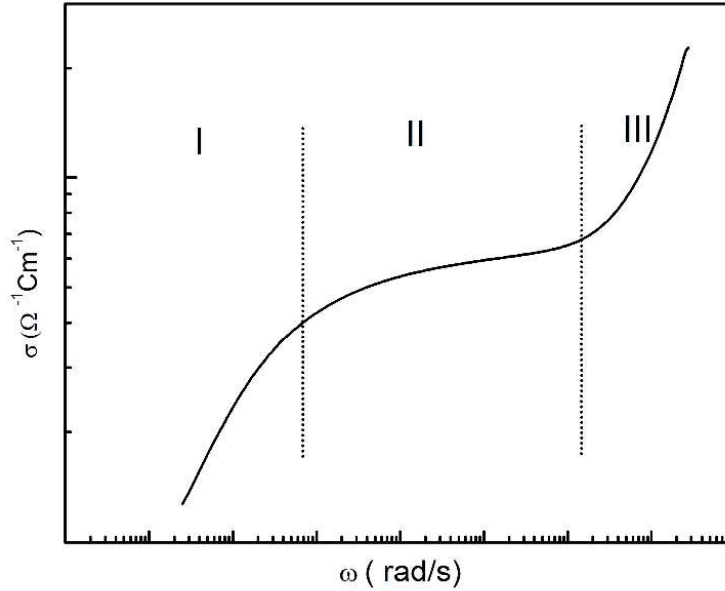
Figure 2.10. *Typical σ' - ω plot for ionic conducting SPEs. Range of spectrum lies from mHz to MHz.*

The Almond west formalism [22] is a modified equation of JPL to define the hopping rate for materials that do not exhibit frequency-independent conductivity plateau. Thus using Almond west formalism, hopping rate (ω_p) were defined as

$$\sigma\ (\omega) = \sigma_{dc}\ [1 + (\frac{\omega}{\omega_p})^n] \qquad (12)$$

An ion-conducting sample is considered as a parallel combination of a lossy/leak capacitor (C) with resistance (R), and its impedance is described ideally as following:

$$Z^* = \frac{R/_{i\omega C}}{R + \frac{1}{i\omega C}} \qquad (13)$$

On simplifying,

$$Z' = \frac{R}{1 + (\omega C R)^2} \text{ and } Z'' = \frac{\omega C R^2}{1 + (\omega C R)^2}$$

On eliminating ω by solving the above two equations, one gets,

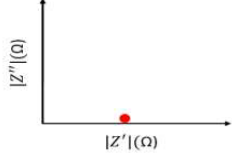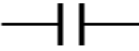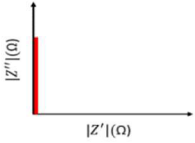$$\left(Z' - \frac{R}{2}\right)^2 + Z'' = \frac{R^2}{4} \qquad (14)$$
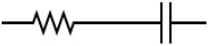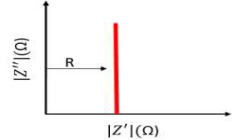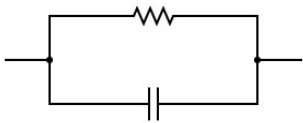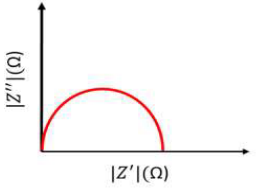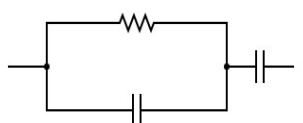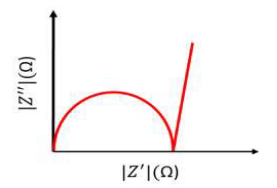
Thus, the Nyquist plot (Z' versus Z″) exhibits a perfect semicircle with its center on the real axis. The diameter of such a semicircle determines the resistance of the material. However, due to the presence of polarization and charge transport a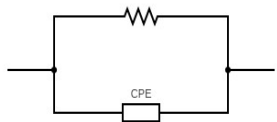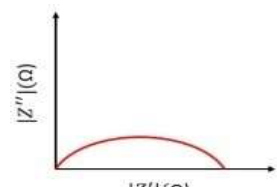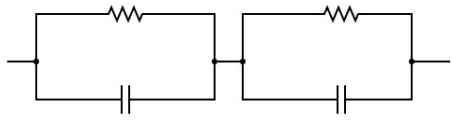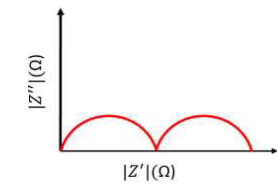t the interface of the grain boundaries, a depressed semicircle was obtained for the composites. Thus, instead of a capacitor, a constant phase element (CPE) [21] in parallel combination with a resistor (R) was used to fit the Nyquist plot. Where the constant phase element is defined by the equation

$$Z_{CPE} = \frac{Z_O}{(i\omega)^\alpha} \quad (15)$$

Here, α lies between 0 and 1. When $\alpha = 0$, Z_{CPE} becomes frequency independent and CPE becomes a pure resistor as $Z_O = R$. On the other hand, when $\alpha = 1$, Z_{CPE} is written as $\frac{Z_O}{i\omega}$ with Z_0 becoming $\frac{1}{C}$. Here CPE acts as a pure capacitor with impedance as *1/iωC*. CPE behaves as an intermediate between a resistor and a capacitor for all other values of α lying between 0 and 1. However, based on the ion transport mechanism in the composites, various components can be designed to fit the Nyquist plot. Some of the configurations are given below. In the present work, EIS impedance analysis software was used for fitting various models (Table 2.2).

Table 2.2 Various possible impedance models that can be applied to various samples as per their electrical properties.

Electrical circuit	Z^*	Plot
—W—	R	
—||—	$\dfrac{1}{i\omega C}$	
—W—||—	$R + \dfrac{1}{i\omega C}$	

Circuit	Equation	Plot
	$\left(Z_R - \dfrac{R}{2}\right)^2 + Z_I^2 = \left(\dfrac{R}{2}\right)^2 = Z_a$	$|Z''|(\Omega)$ vs $|Z'|(\Omega)$
	$Z^2 + \dfrac{1}{(i\omega C)^2}$	$|Z''|(\Omega)$ vs $|Z'|(\Omega)$
	$\dfrac{1}{R} + \dfrac{1}{A(2\pi if)^{-n}}$	$|Z''|(\Omega)$ vs $|Z'|(\Omega)$
	$Z_1 + Z_2$	$|Z''|(\Omega)$ vs $|Z'|(\Omega)$

2.3.8. Transient ionic current (TIC) and ac-dc technique:

To understand the ionic mobility and transference number of the composites, a conventional transient ionic current technique (TIC) developed by Watanabe et. al. [23] and others groups were adopted. In this, a sample sandwiched between two blocking electrodes is polarized for a sufficiently long time using a constant dc potential (0.5 V) typically below the decomposition potential of the sample. The polarity of the applied potential is subsequently reversed, and the current in the circuit (that exhibits a peak) is monitored with time using computer-interfaced high-resolution digital multimeter (Keysight 31446A). Time of flight (τ) is thus measured from the peak in transient current versus time curve as defined in Fig. 2.11a. Using relation $\mu = d^2/V\tau$, mobility (μ) values of the composites is obtained, where d and V are thickness and applied

potential, respectively. Since in the case of SPEs the thickness of the sample is quite small, thus the measurements were done on at least five samples to reach close to accuracy.
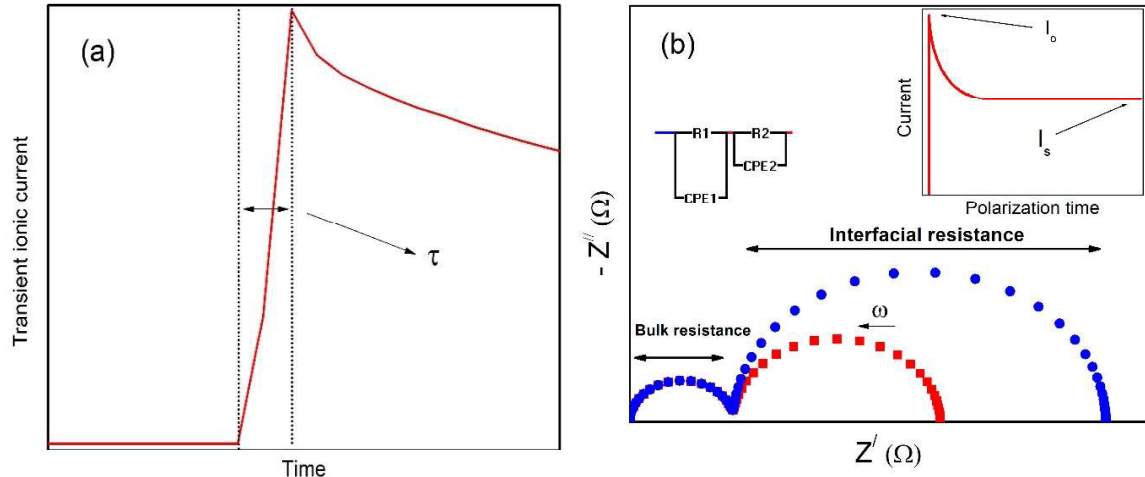
Figure 2.11 *(a) A typical graph of the transient ionic current behaviour with polarization time. (b) Schematic Nyquist plot for cell with before and after polarization along with polarization current with time.*

To elucidate the role of cations in the conductivity rise of the NASICON polymer hybrids, cation transport number ($t_{Li+/Na+}$) was measured by using the conventional ac-dc combined technique [24]. In this, coin cells (2032 type) with a configuration of Li|sample|Li or Na|sample|Na were fabricated in a high purity argon gas atmosphere (impurity ≤ 0.01ppm) in a glove box (MTI Corporation, VGB-1). The Nyquist (Z'-Z'') plots of the cell before and after ~ 3h polarization was obtained, and thus, $t_{Li+/Na+}$ was calculated using the equation

$$t_+ = \frac{I_{ss}\,(V - I_O R_O)}{I_O\,(V - I_{ss} R_s)} \qquad (16)$$

Where I_o is observed peak current (at t = 0), I_{ss} the saturated current, V the applied polarization voltage, R_o the interfacial resistance (noted before polarization), and R_s denotes interfacial resistance immediately measured after ~ 3 h of polarization. Values of R_o and R_s are obtained from Nyquist plots i.e. from the diameter of low-frequency semicircles corresponding to electrode-electrolyte interface (as shown in Fig. 2.11b).

2.3.9. Electrochemical performance

Three main techniques are mostly used for electrochemical characterization of electrolytes/electrodes or devices. These are linear sweep voltammetry (LSV), cyclic voltammetry (CV) and for devices particularly, the galvanostatic charge-discharge (GCD). CV/LSV is about varying potential against time and measuring the current. GCD deals with applying a current with time and measuring voltage.

A three-electrode setup is used for these measurements viz. working, counter, and reference electrodes [25]. While the reference electrode voltage is maintained constant, at the working electrode/test electrode, reduction/oxidation takes place [25]. Further counter (also known as auxiliary) electrode serves as source/sink of electrons [25] and the current from the external circuit is passed through it. The use of these three electrodes particularly in highly conducting liquid electrolytes makes the concurrent measurement of current and voltage accurate. A schematic diagram is shown in Fig 12a. However, by joining reference and counter electrodes, one can also convert the system to a two probe geometry, mainly used for studying solid electrolytes/sandwich geometry cells, as shown in Fig. 2.12b.
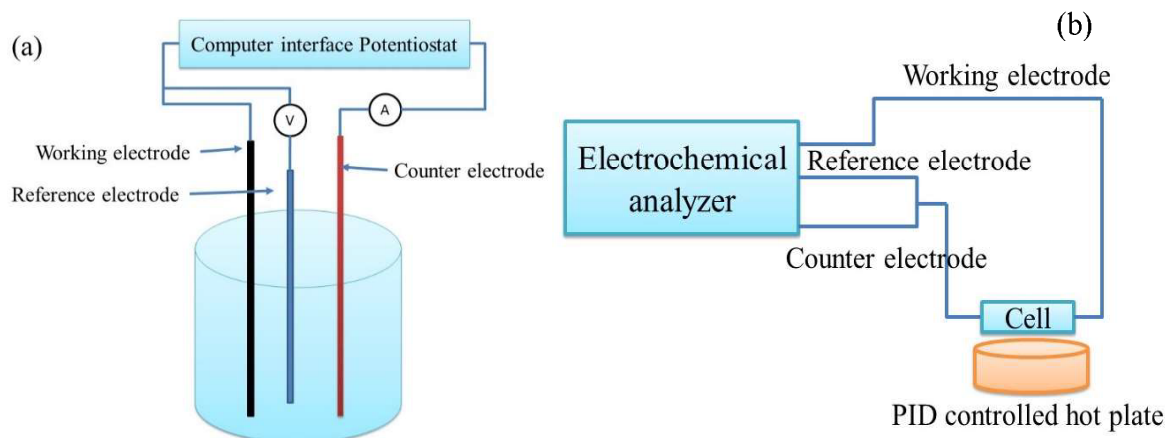

Figure 2.12 *(a) Block diagram of CV setup. (b) Block diagram of the two probe measurement of electrochemical performance*

Linear sweep voltammetry: The electrochemical stability window of the composites was studied using reversible as well as blocking electrodes [26]. To understand the electrolyte decomposition potential, the cell was prepared by sandwiching the composites between blocking electrodes i.e. silver (Ag). Similarly, to understand the potential stability of the

composites with Li/Na metal, symmetric cells of type Na|Sample|Na were prepared and measured the potential breakdown where the current shows an abrupt rise as shown in Fig. 2.13a.
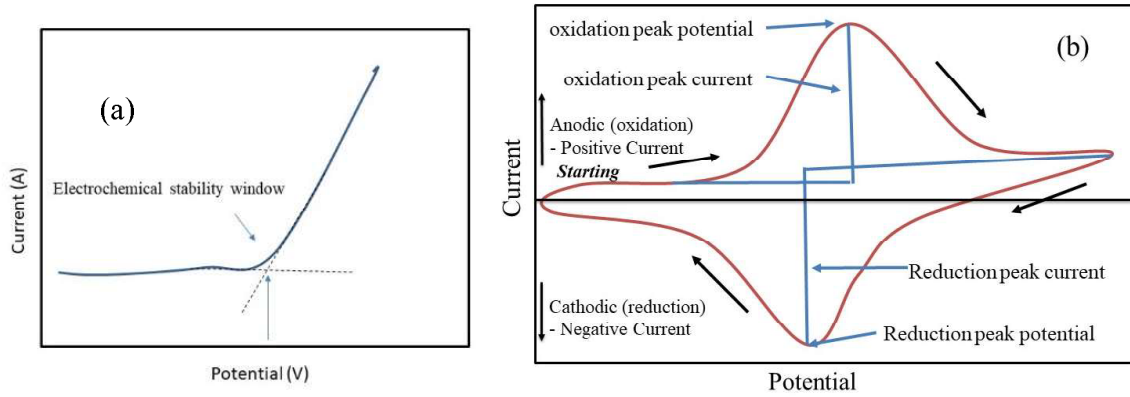
Figure 2.13. *(a) A typical LSV curve showing ESW. (b) Typical CV curve for redox reaction.*

Cyclic voltammetry (CV): As shown in the Fig. 2.13a, oxidation/reduction, ECS window, and chemical (reaction) events can be studied. As per convention, a peak appearing in the direction of increasing voltage is considered oxidation. In the present study, the CV scan was carried out to understand the formation of electric double layer supercapacitor (EDLC) and their operating voltage. Also, their stability was studied by cycling the cell with various scan rates. A typical result of the CV scan for the composites is shown in Figure. Also, in device configuration, from the CV scan, the specific capacitance of the composites was calculated using the equation.

$$C = \frac{Q}{mV} = \frac{I}{m\left(\frac{V}{t}\right)} \quad (17)$$

Where V/t is the voltage scan rate and is represented as K, I is the corresponding current, and m is the mass of a single electrode. Equation (17) can be written as follows;

$$I = C \times m \times K \quad (18)$$

In CV curve, the current changes by changing the potential from V_1 to V_2. Therefore, equation (18) can be written as

$$\int_{V1}^{V2} I(V)dV = \int_{V1}^{V2}(Cp \times m \times K)dV \quad (19)$$

$\int_{V1}^{V2} I(V)dV$ refers to the area under the CV curve. Therefore, specific capacitance can be calculated for the CV curve by the following equation:

$$Cp = \frac{Area\ under\ CV\ curve}{(V2-V1)mK} \qquad (20)$$

Galvanostatic charging-discharging (GCD): Galvanostatic Charge-Discharge (CCD) is a versatile standard technique used to test the performance and cycle-life of EDLCs and batteries. In this technique, a repetitive loop of charging and discharging is monitored. Most often, charge and discharge were conducted at a constant current until a set voltage is reached. The set operating voltage of the cell are generally optimized from the LSV scan. In the present study, the GCD cycles were carried out to study the EDLC/Pseudo SC performance. A typical result of the GCD cycle is shown in Fig 2.14.
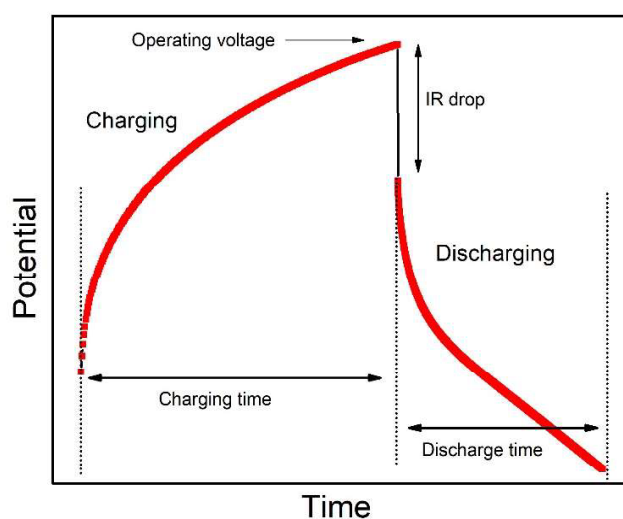
Figure 2.14. *A typical charge-discharge curve for SPEs.*

In most of the case, while discharging a small voltage drop is observed due to equivalent series resistance (ESR) of the current collector and electrode contact. The ESR value provides the details of contact resistance and thus can be used to study the interfacial charge transport reactance. The ESR with current density is calculated using the equation define below.

$$ESR = \frac{Voltage\ drop\ (marked\ as\ IR\ drop\ in\ graph)}{Discharg\ Curent}$$

Also, the specific capacitance (F-g^{-1}) for a single cathode and Specific energy (Wh kg^{-1}) and specific power (W kg^{-1}) for the device is calculated from the charging-discharging curve by considering the following Equations, also reported elsewhere.

$$\text{Specific capacitance (C}_\text{s}) = \frac{2I\,\Delta t}{m\Delta V}$$

$$\text{Specific energy (E}_\text{s}) = \frac{Cs\Delta V^2}{7.2}$$

$$\text{Specific power (P}_\text{s}) = \frac{3600E_s}{\Delta t}$$

Where I is the constant discharge current, Δt the discharging time, ΔV the voltage window excluding IR drop, and m is the average weight of the active material deposited on a single electrode.

Next chapter onwards systematic discussion on different systems is presented.

Reference:

[1]   S. Wang, L. Ben, H. Li, L. Chen, Identifying Li+ ion transport properties of aluminum doped lithium titanium phosphate solid electrolyte at wide temperature range, Solid State Ionics. 268 (2014) 110–116. https://doi.org/10.1016/j.ssi.2014.10.004.

[2]   M. Samiee, B. Radhakrishnan, Z. Rice, Z. Deng, Y.S. Meng, S.P. Ong, J. Luo, Divalent-doped Na3Zr2Si2PO12 natrium superionic conductor: Improving the ionic conductivity via simultaneously optimizing the phase and chemistry of the primary and secondary phases, J. Power Sources. 347 (2017) 229–237. https://doi.org/10.1016/j.jpowsour.2017.02.042.

[3]   K. Kwatek, J.L. Nowiński, Electrical properties of LiTi2(PO4)3and Li1.3Al0.3Ti1.7(PO4)3solid electrolytes containing ionic liquid, Solid State Ionics. 302 (2017) 54–60. https://doi.org/10.1016/j.ssi.2016.11.020.

[4]   Z. Xue, X. Xie, Poly(ethylene oxide)-based electrolytes for lithium-ion batteries, (2015) 19218–19253. https://doi.org/10.1039/c5ta03471j.

[5]   Z. Zhang, K. Xu, X. Rong, Y.S. Hu, H. Li, X. Huang, L. Chen, Na3.4Zr1.8Mg0.2Si2PO12 filled poly(ethylene oxide)/Na(CF3SO2)2N as flexible composite polymer electrolyte for solid-state sodium batteries, J. Power Sources. 372 (2017) 270–275. https://doi.org/10.1016/j.jpowsour.2017.10.083.

[6]   J. Wang, S. Kaskel, KOH activation of carbon-based materials for energy storage, J. Mater. Chem. 22 (2012) 23710–23725. https://doi.org/10.1039/c2jm34066f.

[7]   J. Romanos, M. Beckner, T. Rash, L. Firlej, B. Kuchta, P. Yu, G. Suppes, C. Wexler,

P. Pfeifer, Nanospace engineering of KOH activated carbon, Nanotechnology. 23 (2012). https://doi.org/10.1088/0957-4484/23/1/015401.

[8]   A. Subagio, Y. Al Hakim, M.W. Ristiawan, M.A. Kholil, Priyono, Structural and morphological properties of MnO2/MWCNT composite grown using the hydrothermal method for supercapacitor application, Int. J. Electrochem. Sci. 14 (2019) 9936–9947. https://doi.org/10.20964/2019.10.52.

[9]   G.P. Pandey, S.A. Hashmi, R.C. Agrawal, Hot-press synthesized polyethylene oxide based proton conducting nanocomposite polymer electrolyte dispersed with SiO2 nanoparticles, Solid State Ionics. 179 (2008) 543–549. https://doi.org/10.1016/j.ssi.2008.04.006.

[10]   W. Stark, W. Bohmeyer, 7 - Non-destructive evaluation (NDE) of composites: using ultrasound to monitor the curing of composites, in: V.M.B.T.-N.-D.E. (NDE) of P.M.C. Karbhari (Ed.), Woodhead Publ. Ser. Compos. Sci. Eng., Woodhead Publishing, 2013: pp. 136–181. https://doi.org/https://doi.org/10.1533/9780857093554.1.136.

[11]   S.K. Fullerton-Shirey, J.K. Maranas, Structure and mobility of PEO/LiClO4 solid polymer electrolytes filled with Al2O3 nanoparticles, J. Phys. Chem. C. 114 (2010) 9196–9206. https://doi.org/10.1021/jp906608p.

[12]   A. Mayeen, L.K. Shaji, A.K. Nair, N. Kalarikkal, Morphological characterization of nanomaterials, in: Charact. Nanomater. Adv. Key Technol., Woodhead Publishing, 2018: pp. 335–364. https://doi.org/10.1016/B978-0-08-101973-3.00012-2.

[13]   J.E. Penner-Hahn, X-ray Absorption Spectroscopy, in: Compr. Coord. Chem. II, 2003: pp. 159–186. https://doi.org/10.1016/B0-08-043748-6/01063-X.

[14]   C.D. Garner, X-ray absorption spectroscopy, Nature. 277 (1979) 89–90. https://doi.org/10.1038/277089a0.

[15]   R. Article, X-Ray Absorption Fine Structure (XAFS) Spectroscopy – A Review, (2013) 921–966.

[16]   M. Aziz, A.F. Ismail, X-Ray Photoelectron Spectroscopy (XPS), Elsevier B.V., 2017. https://doi.org/10.1016/B978-0-444-63776-5.00005-X.

[17]   V.I. Bukhtiyarov, M. Hävecker, V. V Kaichev, A. Knop-Gericke, R.W. Mayer, R. Schlögl, X-ray absorption and photoemission studies of the active oxygen for ethylene

epoxidation over silver, Catal. Letters. 74 (2001) 121–125.
https://doi.org/10.1023/A:1016666021405.

[18]   Jagannath, U.K. Goutam, R.K. Sharma, J. Singh, K. Dutta, U.S. Sule, R. Pradeep, S.C.
Gadkari, HAXPES beamline PES-BL14 at the Indus-2 synchrotron radiation source, J.
Synchrotron Radiat. 25 (2018) 1541–1547.
https://doi.org/10.1107/S1600577518008408.

[19]   E.P. Barrett, L.G. Joyner, P.P. Halenda, The Determination of Pore Volume and Area
Distributions in Porous Substances. I. Computations from Nitrogen Isotherms, J. Am.
Chem. Soc. 73 (1951) 373–380. https://doi.org/10.1021/ja01145a126.

[20]   A.K. Jonscher, Dielectric relaxation in solids, J. Phys. D. Appl. Phys. 32 (1999).
https://doi.org/10.1088/0022-3727/32/14/201.

[21]   J.R. Macdonald, Impedance spectroscopy: Models, data fitting, and analysis, Solid
State Ionics. 176 (2005) 1961–1969.
https://doi.org/https://doi.org/10.1016/j.ssi.2004.05.035.

[22]   D.P. Almond, C.C. Hunter, A.R. West, The extraction of ionic conductivities and
hopping rates from a.c. conductivity data, J. Mater. Sci. 19 (1984) 3236–3248.
https://doi.org/10.1007/BF00549810.

[23]   M. Watanabe, K. Sanui, N. Ogata, T. Kobayashi, Z. Ohtaki, Ionic conductivity and
mobility in network polymers from poly(propylene oxide) containing lithium
perchlorate, J. Appl. Phys. 57 (1985) 123–128. https://doi.org/10.1063/1.335386.

[24]   W. Liu, S.W. Lee, D. Lin, F. Shi, S. Wang, A.D. Sendek, Y. Cui, Enhancing ionic
conductivity in composite polymer electrolytes with well-aligned ceramic nanowires,
Nat. Energy. 2 (2017). https://doi.org/10.1038/nenergy.2017.35.

[25]   N. Elgrishi, K.J. Rountree, B.D. McCarthy, E.S. Rountree, T.T. Eisenhart, J.L.
Dempsey, A Practical Beginner's Guide to Cyclic Voltammetry, J. Chem. Educ. 95
(2018) 197–206. https://doi.org/10.1021/acs.jchemed.7b00361.

[26]   C.F.N. Marchiori, R.P. Carvalho, M. Ebadi, D. Brandell, C.M. Araujo, Understanding
the Electrochemical Stability Window of Polymer Electrolytes in Solid-State Batteries
from Atomic-Scale Modeling: The Role of Li-Ion Salts, Chem. Mater. 32 (2020)
7237–7246. https://doi.org/10.1021/acs.chemmater.0c01489.